Study of hadrons at the cores of extensive air showers and the elemental composition of cosmic rays at 10^{15} eV

H. T. Freudenreich,* A. I. Mincer,† D. Berley,‡ J. A. Goodman, S. Tonwar,§
A. Wrotniak,* and G. B. Yodh**
University of Maryland, College Park, Maryland 20742

R. W. Ellsworth
George Mason University, Fairfax, Virginia 22030
(Received 11 September 1989)

An experiment was done near sea level at College Park, Maryland, to study hadrons near the cores of air showers resulting from primary cosmic rays of 100–10 000 TeV per nucleon. The parameters studied were (1) the rate of events which exceed a minimum shower density cut and specific hadronic calorimeter signal cuts and (2) the rate of events with hadrons delayed with respect to the shower front. Extensive computer simulations of the experiment were done using several particle-interaction and primary-composition models as well as details of the detector response. It is found that interaction models which include scaling or only modest scaling violation will fit the data only with primary spectra that are rich in heavy nuclei in the 100–10 000-TeV total-energy range. A proton-dominated flux will fit the data only when an extreme scale-breaking model is used, in disagreement with extrapolations of accelerator data.

I. INTRODUCTION

An experiment was performed near sea level at College Park, Maryland to study hadrons near the cores of air showers resulting from primary cosmic rays of 100–10 000 TeV per nucleon. This paper reports results on the spectrum and composition of cosmic rays near 1000 TeV. An analysis of the temporal structure of the hadronic component in a search for unknown massive particles was previously reported.[1] Several years ago a similar experiment, but at mountain altitude, was completed and the results published.[2] The present experiment, since it is at a greater atmospheric depth, is sensitive to higher-energy primaries.

The apparatus consisted of 12 scintillation counters to sample the density of electrons and four ionization calorimeters to sample hadrons. The characteristics of the data studied were (1) the rate at which events exceeded thresholds of shower density and energy deposited in the calorimeters (the trigger rate) and (2) the temporal spectrum of hadrons with respect to the main front of the shower (the rate of delayed hadrons). These measurements were compared with extensive computer simulations of the apparatus and the propagation of showers induced by primary-cosmic-ray nuclei of several atomic masses.[3,1]

The results, combined with simple extrapolations from existing accelerator data, require the presence of a heavy component in the primary-cosmic-ray spectrum and rule out hydrogen and helium as the only components of cosmic rays at an energy of about 1000 TeV.

Only a few experiments sample primary cosmic rays above 10^{12} eV and provide direct identification of the primary particle and measurement of its energy. The balloon-borne apparatus of the JACEE Collaboration (Japan American Collaborative Emulsion Experiment)[4] has measured the integral spectrum of the proton flux with energy greater than E to be falling according to a power law,[5] $E^{-\Gamma}$, with a constant integral spectral index ($\Gamma=1.81\pm1.3$) from 10^{11} to 10^{13} eV. These and similar results for helium are consistent with extrapolations of earlier, lower-energy measurements.[6,7] Until recently, measurements of the flux of nuclei heavier than helium were only available for energies less than 10^{12} to 10^{13} eV per nucleus but recent JACEE results extend the measurements to about 10^{14} eV nucleus.[8] Except at the higher energies where the JACEE experiment is statistically limited by the available flux, the proportion of heavy particles is much less than the proportion of hydrogen or helium and the heavy particle spectra all fall with energy with a constant spectral index slightly less than the indices for hydrogen and helium. These data and the all-particle spectrum are summarized by Balasubrahmanyan *et al.*[9] The all-particle spectrum measured up to 10^{16} eV by Grigorov *et al.*[10] is the highest-energy direct measurement. From 10^{12} to 10^{15} eV the all-particle spectrum follows a power law with a constant spectral index ($\Gamma=1.62\pm0.02$). The all-particle spectrum steepens between 10^{15} and 10^{16} eV. Recently two other experiments have made measurements of primary-cosmic-ray spectra for elements heavier than protons and alphas. The Chicago Cosmic Ray Nuclei Experiment[11] (CRNE) in the space shuttle and the Goddard Space Flight Center balloon-borne experiment[12] (HEGCS) obtained spectral indices for CO (carbon and oxygen), silicon-group, and iron-group elements up to several hundred GeV/nucleon. The CRNE group finds a large index for the differential spectrum of silicon ($\gamma=2.97\pm0.12$) and a value con-

 ©1990 The American Physical Society

sistent with previous measurements for C and O. For the Fe group CRNE finds a spectral index of $\gamma = 2.55 \pm 0.09$, consistent with the results of HEGCS.

The observed steepening (bend) of the all-particle spectrum is explained differently by different models of cosmic-ray origin, acceleration, and propagation. These models make different predictions of cosmic-ray composition near the bend. Direct measurements of individual elements are made at energies below the steepening in the all-particle spectrum and therefore give no information on the mechanism responsible for the bend.

Indirect measurements, that is, measurements of the air showers initiated by primary cosmic rays, have the advantage of sensitivity to smaller flux and therefore can detect primaries of higher energy than the direct measurements. They are difficult to interpret and lead to contradictory results with regard to the composition and nature of particle interactions at these high energies.[13] Some examples are (a) the use of equal-frequency contours in the variables electron-shower size and zenith angle to trace out the longitudinal distribution of shower development with depth,[14] (b) γ-ray families at mountain altitude,[15] (c) electron-muon number correlations,[16] and (d) energy or size variation of depth of shower maximum.[17]

Some authors have suggested that observed changes in air-shower properties near the bend are due to changes in particle-interaction properties while others attribute them to changes in composition.[13,18]

The analysis of this paper is different than previous studies. Extensive simulations were done for a variety of composition models, several interaction models, *and* the response of the detector to the hadronic and leptonic component of the cosmic-ray shower. The measured trigger rate and temporal distribution of hadrons delayed with respect to the shower front provide new information about the primary composition at energies where direct measurements exist and where the all-particle spectrum steepens.

Since fluctuations dominate in the trigger, the sensitivity of this experiment to elemental composition can be demonstrated only through Monte Carlo simulation. The process involves several competing factors. Showers from light primaries observed at sea level have fewer hadrons but more high-energy hadrons than do showers from heavy primaries at the same total energy. Showers from light primaries are less laterally spread and are more penetrating than are showers from heavy primaries. Monte Carlo simulations show that the more penetrating light primary showers are more likely to trigger our detector than are showers from heavy primaries of the same energy. On the other hand, the more spread out and more low-energy hadron showers from heavy primaries are more likely to produce events with hadrons delayed with respect to the shower front. The trigger and delay rates are therefore sensitive to primary composition. Simulations show that the shower density distribution, hadron energy distribution, and lateral spread of the measured hadronic component (as measured in this experiment) are insensitive to primary composition.

II. THE EXPERIMENTAL APPARATUS

The experiment was located in and around a thin-roofed shack and adjacent to a counting-house trailer near sea level on the University of Maryland campus in College Park, Maryland. It is shown schematically in Fig. 1. The apparatus consisted of four iron and lead calorimeters and an array of 12 scintillation counters distributed over an area of about 200 m^2. The calorimeters were used to sample hadronic energy and the 12 shower counters to measure the density of electrons in the showers. Signal size and arrival time were recorded for each counter.

Each of the four calorimeters consisted of layers of scintillation counters placed horizontally and separated by lead or iron. Each calorimeter had an active area of 1.2 m $\times$ 1.2 m and was segmented into four quadrants. Two separate configurations were used for the vertical profile of the scintillators; they are shown in Fig. 2. The counters in the *A*, *T*, *B*, *C*, and *E* layers were $\frac{1}{2}$-in. plastic scintillators viewed by fast photomultiplier tubes of 2 in. diameter (RCA 8575) through plastic light guides. The *D*-layer counters were 3-in.-thick plexiglass containers filled with liquid scintillator (Shell 63702 mineral oil, mineral-based scintillator Pilot P5007, and a wave shifter). Each *D*-layer counter was viewed by two 2-in. phototubes (RCA 6655A) directly coupled to the container. A border of 10 in. of steel and lead extended beyond the counters in the calorimeter to shield from particles entering from the side.

The eight shower counters located around the calorimeters were liquid scintillators identical to the *D* counters. The four *A* counters used to measure shower density and timing were located directly on top of the calorimeters.

The signal from each counter was fed to a passive fan out and then to an analog-to-digital converter (ADC), where the charge was digitized. The signals from all of

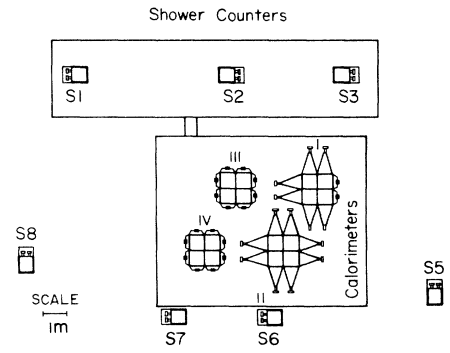

FIG. 1. Plan view of the experimental apparatus. The hadron calorimeters I through IV were located inside a thin-roofed shack. Scintillation counters S1 and S8 are shown. Four more scintillation counters (*A* counters) were located over the calorimeters. Counters S1, S2, and S3 were located on the roof of a trailer housing the electronics and data-acquisition equipment.

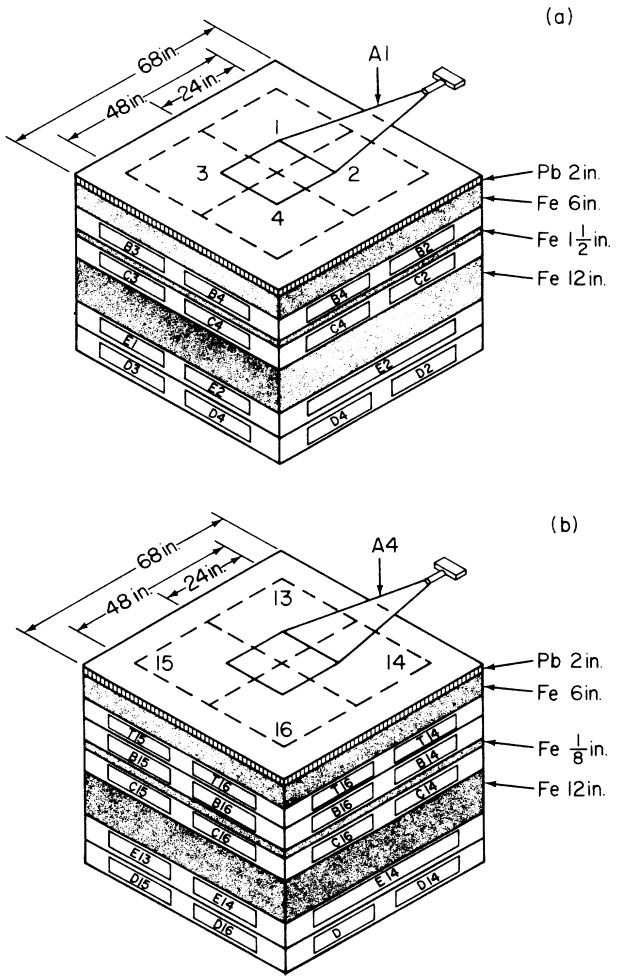

FIG. 2. Detail of the construction of the calorimeters I through III (a) and calorimeter IV (b).

the counters except the *D*'s were also sent to discriminators and then to time-to-digital converters (TDC's) where the time of arrival of the first pulse in each channel was recorded. The threshold for firing the TDC was set so that a signal of integrated charge of greater than 0.1 equivalent particles in an *A* or *E* counter had its time recorded with high efficiency. In order to prevent fast muons accompanying the air shower from stopping the timing signal in the calorimeters, the thresholds for *T*, *B*, and *C* counters were set to three equivalent particles. In that way hadronic signals arriving later were infrequently vetoed by a single muon.

All recorded events satisfied a set of on-line trigger requirements: (1) the summed signals from the *B* and *C* layers from at least one calorimeter were greater than 70 equivalent particles (energy sum condition) and (2) at least two of the *A* counters had a signal greater than 0.1 particles and fired the TDC discriminator. The master trigger was fired at the instant the above conditions were met. Hadronic signals arriving from 140 ns before to 130 ns after the shower signal in the *A* counters were recorded. The trigger electronics is shown diagrammatically in Fig. 3.

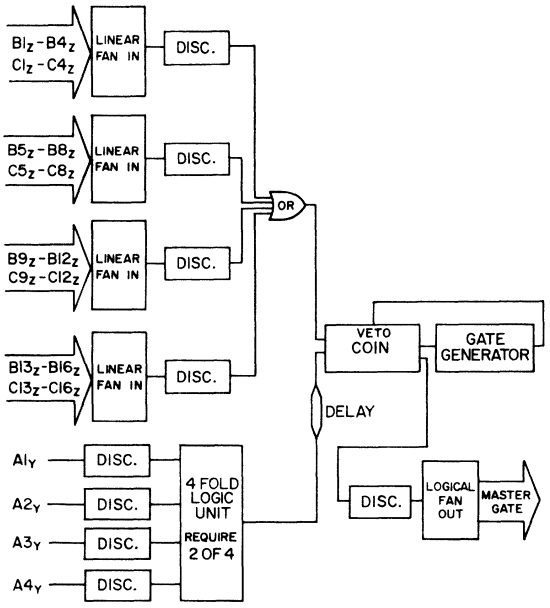

FIG. 3. Logic of the experimental trigger electronics.

The master trigger initiated the digitization of the charge in each counter and its time of arrival. The timing sequence is shown in Fig. 4. The master gate used for charge digitization opened 50 ns before a prompt signal arrived at the ADC and lasted for 250 ns. The master trigger also started the TDC's. Delays were arranged so that a prompt signal stopped the TDC 50 ns after it start-

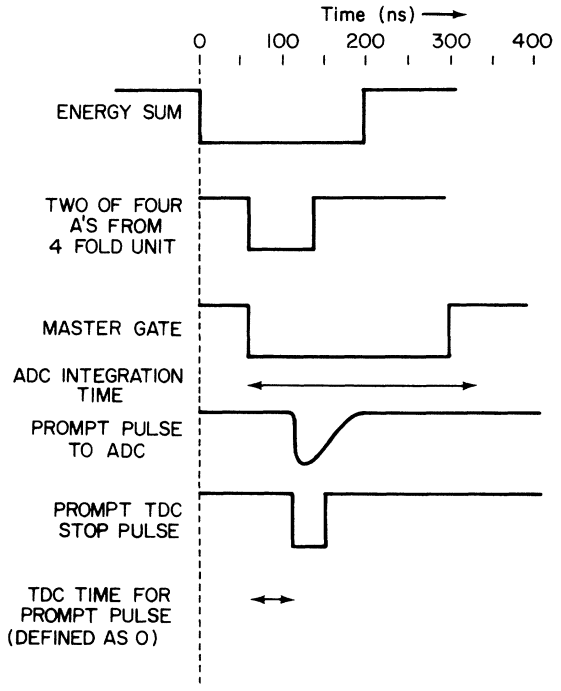

FIG. 4. Temporal sequence of events for prompt triggering of the energy sum.

ed. The dynamic range of the TDC was 340 ns and provided a time range from −50 ns to +290 ns with respect to a prompt signal. The master trigger also sent an interrupt to an 8080 microprocessor which read the digitized data and wrote it on magnetic tape.

The timing resolution is found by studying the distribution of the difference between the times of arrival of signals in the *A* counters and the *B* and *C* counters below them. Figure 5 shows these difference plots as a function of *B* and *C* counter signal. These plots show that the resolution for events with large signals in the *B* and *C* counters is 3 ns. These plots also show a systematic shift toward later *B* and *C* times for small signal events. This effect is due to the rise time of the phototube pulses and slewing in the electronics. There is also evidence of an early peak in Fig. 5(a). This peak, due to pulses of low integrated charge, was studied by observing pulses from particles which penetrated the calorimeter. It was found that the early peak in Fig. 5(a) can be explained by signals which exceed the amplitude threshold of the TDC discriminator by being fast rising. These fast-rising pulses of low integrated charge will not be slewed. A significant tail of late-arriving signal which is evident in these figures is associated with the properties of the showers and will be discussed in detail below.

The on-line data-collection system was also used for monitoring and calibration. Continuous monitoring of the performance of the experiment was done by accumulating on-line histograms of all counters and studying them daily.

Gain shifts were monitored with weekly calibrations. The automatic calibration system to monitor gains employed through-going particles as defined by the *A* and *E* counters. The computer determined the median-to-

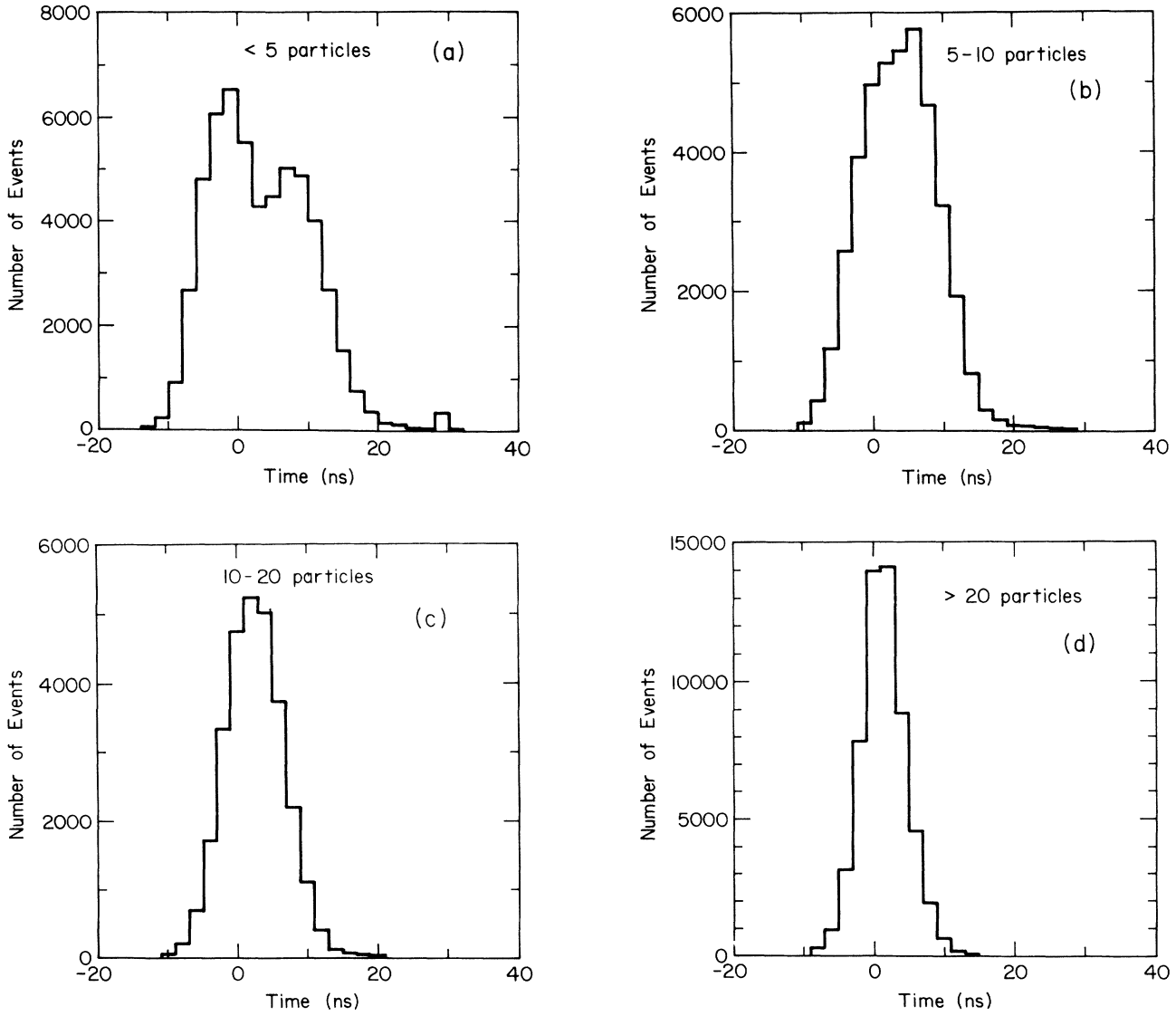

FIG. 5. Distributions of the difference between the times of signals in the *A* counters and the *B* and *C* counters below them for *B* and *C* signals of (a) less than five equivalent particles, (b) 5–10 equivalent particles, (c) 10–20 equivalent particles, (d) greater than 20 equivalent particles.

pedestal difference, typically 20 channels, for the mean signal distribution of each counter. This was used as the definition of an equivalent particle. In order to achieve good resolution while calibrating without sacrificing dynamic range, a switchable attenuator (a factor of 10) was in place during data taking and removed during calibration. The gains typically varied less than 5% per week and the pedestals varied less than one channel per week and three channels per year. The ADC dynamic range allowed observations of signals in the *B* and *C* counters of from 0.5 to 500 equivalent particles. The response of the phototubes to input light was measured and found to be linear up to 350 equivalent particles.

III. THE DATA

In 12 500 h of total on time, the master trigger initiated 240 000 events which were recorded on tape. The apparatus had a dead time which depended upon the previous event history. After an event was registered, the software could not process a second event for 4 msec and a third event for 30 sec. The live time was 97.6% of the run time.

For the part of the experiment involving the analysis of the rate at which events exceeded the thresholds of shower density and energy deposited in the calorimeters, the following off-line cuts were made (1) at least one calorimeter had a signal of at least 75 equivalent particles and (2) the shower density as measured by the *A* counters was at least ten equivalent particles per square meter, These cuts were satisfied by 46 448 events, corresponding to a trigger rate of 3.78 ± 0.05 events per hour.

For the part of the experiment involving the delay in the time of arrival of hadrons with respect to the main front of the shower, a slightly higher cut of 13.6 equivalent particles per square meter was made on the shower density. A larger signal in the *A* counters improved the timing information on the shower. The corresponding trigger rate was 3.15 ± 0.04 events per hour.

Figure 6 shows a scatter plot of measured *B* layer signals and time delays. The bulk of events is approximately centered about 0 ns and is approximately symmetric about 0 for large signals. No counter pulses are earlier than -20 ns, but a large number of events are present with small signals and time delays greater than 20 ns. There are also several counters with large delayed signals. *C*-layer events are similarly distributed.

A delayed event is defined as an event passing the second set of off-line cuts in which at least one calorimeter counter has a pulse height greater than seven equivalent particles and a time delay greater than 20 ns. The signal cut was chosen to avoid the slewing discussed previously, which gives later than true time readings for small-signal particles. The time cut was chosen to avoid delays from the tail of the time resolution. The measured delayed event rate is (0.050 ± 0.004)/h.

IV. SIMULATION OF THE EXPERIMENT

A. Overview of the simulation

This experiment samples the nuclear-electromagnetic cascades induced by cosmic rays. The type of primary

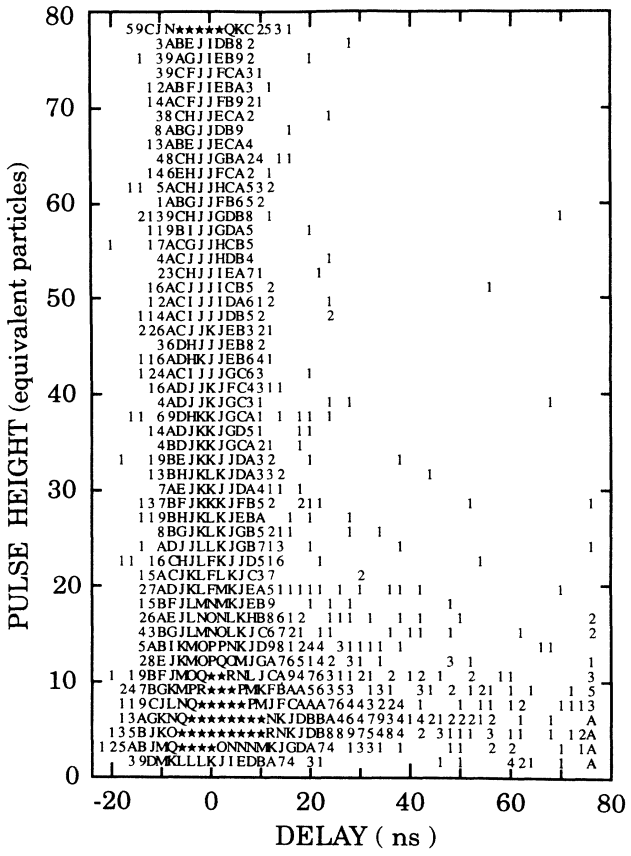

FIG. 6. Scatter plot of measured *B*-layer signals and $(B-A)$ time delays. Overflow bins are at 78 equivalent particles and 76 ns. No underflow events were recorded.

cosmic ray or its energy are impossible to identify in any single event because the fluctuations in shower development are large. In order to study the elemental composition of the primary spectrum the measurements were compared with a simulated ensemble of events. The simulations were done with several interaction and composition models, and with properties of the detector determined in a test beam at low energy and extrapolated to high energy with Monte Carlo calculations. These studies determined the probability of triggering the experiment as a function of primary mass and energy.

Showers were generated using six different models of hadronic interactions, for several species of nuclei: primary mass numbers 1, 14, and 56. They represent hydrogen, the carbon-nitrogen-oxygen group, and the iron group. Results from helium (mass number 4) and the silicon group (mass number 28) were obtained by interpolation. (Showers were also generated for He and Si, but only in sufficient number to assure the validity of the interpolations.) The energy range covered by the simulations was 6.25×10^{12} eV to 1.28×10^{16} eV for hydrogen and 6.25×10^{12} eV/nucleon to 8×10^{14} eV/nucleon for the other species. The energy range of the simulated showers was divided into bins successively doubling in width, i.e., 6.25–12.5, 12.5–25, . . . , 400–800 TeV. Within each bin the energies (E) of the primaries were

selected according to a number spectrum:

$$\frac{dN}{dE} \propto E^{-2.6} .$$

Analysis was carried out for each energy interval individually and the results weighted and combined according to the desired primary spectrum, which was constrained by the measured all-particle flux. The zenith angle was chosen from a distribution uniform in its cosine, from 0° to 45°. 97% of the detected events were contained in this angular interval.

The air showers were generated by a Monte Carlo technique. All particles created in the shower were followed if their energy exceeded 1 or 2 GeV (depending on the model) until they interacted or reached the detector level. The interaction models are described in more detail in Sec. IV C.

For each hadron reaching the atmospheric depth of the detector its coordinates, its energy, its particular type, its arrival time, the local shower density, and the muon density were stored in a grid of cells by position (with a program called GRID). The size of each cell was equal to the size of a single quadrant of a calorimeter. A model of the four calorimeters, consisting of four groups of four adjacent cells, was placed at every position on the grid, so that every cell was occupied once and only once.

At each position this model simulated the effects of the incident hadrons, and of the muons and electromagnetic component of the shower, recorded as densities. The effect of albedo in the A counters from hadronic cascades in the calorimeter, muon contribution to the signals, and signals from the light pipes were included in the simulation, as was the lateral spread of hadronic energy from the spread of the cascade and from knock on neutrons. The GRID program was run for each particle type and energy bin. The simulation of the detector is described in more detail in Sec. IV D.

B. Composition models

This section describes the composition models used in the analysis of the data. There is an infinite number of possible spectra consistent with what is known about the primary flux near 10^{15} eV in the all-particle spectrum. In this paper, five generic models of primary spectra were used. In each of these models the primary flux was represented by five groups of nuclear species: protons, alpha particles and the groups carbon-nitrogen-oxygen (CNO), silicon, and iron. These represent the dominant components of the primary cosmic rays.

In each of the models the differential flux I_i of a component i is assumed to follow a power law:

$$I_i = k_i \epsilon^{-\gamma_i} ,$$

where ϵ is the energy per nucleon and γ_i is the spectral index for the ith species. The models differ in the energy dependence of the spectral index for each species.

The fluxes used to determine the constants k_i are given in Table I. This table was derived from a compilation of direct measurements of the differential.[3,1] The constants used for each of the two parts of the analyses (done at different times) are listed separately: the determination of the primary spectrum from the trigger rate of this experiment and the all-particle spectrum (discussed in Sec. V) and for the determination of the spectrum from the trigger rate and the rate of delayed hadrons (Sec. VI).

For the analysis involving the trigger rate and the all-particle spectrum,[3] the constants k_i were adjusted proportionately so that the all-particle integral flux at 1 TeV equaled that given by a fit to the all-particle spectrum.[10] The adjustment needed to match the two fluxes was typically a few percent.

The first four of the models are described by two parameters: a differential spectral index and an energy (or rigidity) at which the spectral slope steepens. In these models two types of spectra are studied. For the first type (models 1R and 1E), all species have a common spectral index which is allowed to vary. For the second type (models 2R and 2E), proton and helium nuclei have a fixed spectral index given by experiment at low energy, whereas heavier nuclei have a common spectral index which is allowed to vary. For each of these models the spectrum of each species steepens at some rigidity (models 1R and 2R) or energy (models 1E and 2E). These models represent different astrophysical scenarios. A model with common spectral index and a rigidity cutoff is expected to apply if the cosmic rays are stochastically accelerated and escape from the galaxy above some rigidity.[19–23] A total energy cutoff is expected if cosmic rays are destroyed in the source above a certain energy due to catastrophic collisions.[24,25] If the source of the proton and helium components is different from that of heavier components then one expects different spectral indices for proton and helium relative to other species.

In each of the models 1R, 1E, 2R, and 2E, the compo-

TABLE I. Flux used for normalization.

Group	Energy (GeV/nucleon)	Flux ($GeV^{-1}s^{-1}m^{-2}sr^{-1}$) Trigger rate and all-particle spectrum	Trigger rate and delay rate
Protons	100	0.063	0.063
He	100	0.0025	0.0025
CNO	250	2.5×10^{-5}	1.8×10^{-5}
Si	250	6.6×10^{-6}	7.6×10^{-6}
Fe	100	1.1×10^{-5}	1.4×10^{-5}

sition is determined by two parameters, γ and E_c. Parameter γ determines the differential slope or spectral index and E_c the location of the bend in the all-particle spectrum.

The model 2R is the "two-slope, rigidity-cut" spectrum. For the analysis of the trigger rate and the all-particle spectrum (Sec. V) the slope of the proton and helium fluxes is 2.78; the free parameter γ is the common slope of the CNO, silicon, and iron fluxes. For the analysis of the trigger rate and the delayed rate (Sec. VI), $\gamma_p=2.75$, $\gamma_{He}=2.78$, $\gamma_{CNO}=2.6$; the free parameter γ is the slope of the Si and Fe fluxes. The rigidity-cut parameter E_c is the common value of rigidity at which all slopes are incremented by 0.5. For example, if in the case of the analysis involving the trigger rate and the all-particle spectrum $E_c=100$ TV/u, then the proton flux steepens from slope 2.78 to 3.28 at 100 TeV, the helium flux steepens similarly at 200 TeV, and the CNO, silicon, and iron fluxes steepen from γ to $\gamma+0.5$ at energies 700, 1400, and 2800 TeV, respectively. This choice of spectral indices for protons and helium is motivated by the results of the JACEE (Ref. 4) Collaboration: that the proton and helium components of the all-particle flux are steep and constant in slope up to ~ 10 TeV/nucleon; the integral slopes are $\Gamma_p=1.18\pm0.13$ for protons and $\Gamma_{He}=1.83\pm0.2$ for helium nuclei. The flux distributions of heavier nuclei are given a common spectral index obtained from an extrapolation of data from balloon and satellite experiments, with the addition of a rigidity cut. CNO, silicon, and iron may not actually have the same slope, but this ansatz leads to the simplest form of spectrum consistent with the measured flux.

In model 2E the rigidity cut of 2R is replaced by a steepening at a common energy. Here, if E_c equals 100 TeV, then all differential slopes steepen by 0.5 at an energy of 100 TeV. An increase in the spectral index by 0.5 corresponds to the observed steepening of the all-particle spectrum.

The "one-slope" models, 1R and 1E, create a simple, proton-dominant spectrum consistent with the JACEE data. In the 1R (1E) model this is done by giving all species a common spectral index above 5 TV/u (5 TeV). The light nuclei cannot be allowed to vary at a much lower energy where they are directly measured. If they are allowed to vary only at a energies much higher than 5 TV/u (5 TeV), the resulting model would be similar to the two-slope forms already described. In 1R the free parameter E_c is a rigidity cut which functions the same way as in 2R; in 1E it is an energy, as in 2E.

Figures 7 and 8 show examples of the four spectral models. The label of each plot contains the point (E_c,γ) that specifies the spectrum. These particular spectra agree best with data on the all-particle spectrum. How this agreement is measured is the topic of Sec. V.

The fifth model is that proposed by Fichtel and Linsley.[26] They propose that cosmic rays originate from two types of sources: one responsible for the low-energy part of the spectrum, dominating below 10^3 TeV, and a second responsible for the high-energy part of the spectrum, dominating above 10^4 TeV (see Fig. 9). The low-energy spectra of the CNO (the carbon, nitrogen, and oxygen group), silicon, and iron are flatter than that of hydrogen. At 150 GeV/u their spectral indices increase and all elemental components from the "low-energy source" share a common index of $\gamma=2.72$. The flux from the "high-energy" source consists of protons and helium. Nuclei behavior than helium have been removed by fragmentation in material near the source. Two spectral models, differing only in rigidity cut, are considered.

(1) Both the "low-energy" and the "high-energy" sources are distributed through the galactic plane. The bend is universal at 3×10^3 TV/u.

(2) The "low-energy" source is distributed through the galactic plane and the "high-energy" source is at the galactic center perhaps associated with a large black hole. The flux from the "low-energy" source steepens at 5×10^2 TV/u, from the "high-energy" source at 5×10^3 TV/u.

The spectral indices for all species increase by 1.0 at the rigidity cut to give the observed all-particle spectrum.

C. Particle-interaction models

The simulations of this experiment require a description of hadron-nucleus and nucleus-nucleus interactions

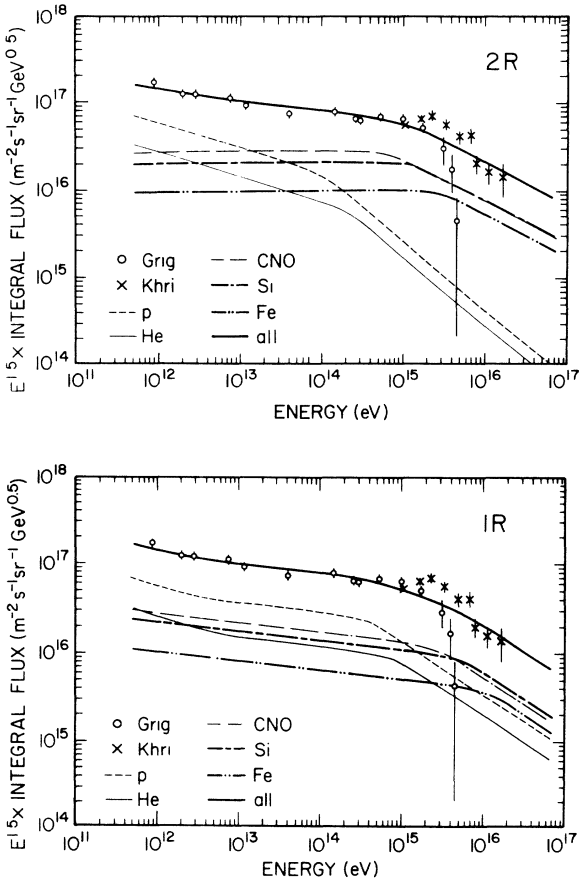

FIG. 7. Best fits of flux with rigidity cut to Grigorov and Khristiansen data. Solid line of each plot is the calculated all-particle flux. Points with error bars are the data of Grigorov *et al.* or Khristiansen *et al.* Top: best fitting 2R flux ($E_c=148$ TV/u, $\gamma=2.49$). Bottom: best fitting 1R flux ($E_c=557$ TV/u, $\gamma=2.60$).

up to energies of 1.3×10^{16} eV, an extrapolation of a factor of 10 in energy (center-of-mass frame) from accelerator measurements of $\bar{p}$-p interactions at the CERN SPS and the Fermilab Tevatron collider, and a factor of 100 from measurements of He-He interactions at the CERN ISR and the CERN SPS experiments with heavier ions. Many extrapolations are possible. Six different models of hadronic interactions were chosen to as to give maximum diversity of extrapolations from existing accelerator data.

Throughout the analysis the six models were identified by the code names Md0, Md1, A00, F00, F2, and Md2. The code for the Maryland model Md0 was written for an earlier experiment done at mountain altitude.[2] Md0 was the only simulation used to analyze the delayed hadron signals.[1] The other models (F00, A00, and F2) use the program SHOWERSIM 84 (Ref. 27) as modified by Freudenreich.[3] The Md1 and Md2 models use the SHOWERSIM code but with many of the features of the Md0 model. The models Md2 and F2 were high-inelasticity models chosen to make nucleon-air interactions appear like heavy nucleus-air interactions. Such models are not consistent with accelerator data (see, for example, Taylor *et al.*[28]).

In all six models secondaries are emitted independently of each other, constrained only by energy and momentum conservation. Momenta of secondary particles are chosen randomly from probability distributions obtained from the invariant inclusive cross section for single-particle production.

In the Maryland models (Md0, Md1, and Md2) the x distributions are chosen in the center-of-mass system while in the SHOWERSIM models all calculations are in the laboratory frame. Secondary particles are created until the available energy is exhausted. A projectile meson or nucleon is assumed to interact with a single nucleon in the air nucleus; the effects of other nucleons in the nucleus are ignored. The general features of the models are summarized in the discussion below.

(i) Cross section. The inelastic nucleus-air cross section is based on the Gaisser and Stanev[29] approximation for all models except Md0:

$$\sigma^{\text{inel}}_{A\,\text{air}}=a+b\ln\left[\frac{F(E)}{38}\right]\text{ mb},$$

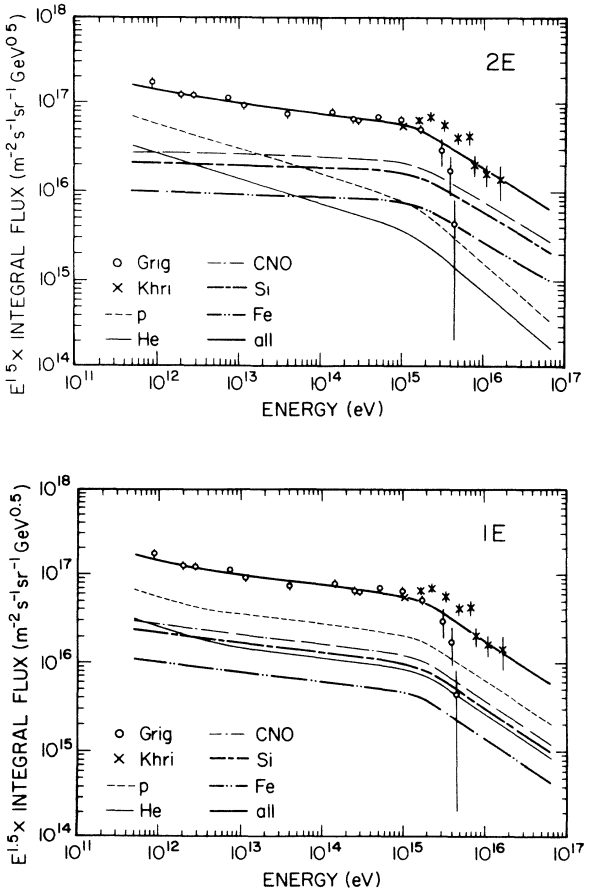

FIG. 8. Best fits of flux with energy cut to Grigorov and Khristiansen data. Solid line of each plot is the calculated all-particle flux. Points with error bars are the data of Grigorov *et al.* or Khristiansen *et al.* Top: best fitting 2E flux ($E_c=2219$ TeV, $\gamma=2.52$). Bottom: best fitting 1E flux ($E_c=2649$ TeV, $\gamma=2.61$).

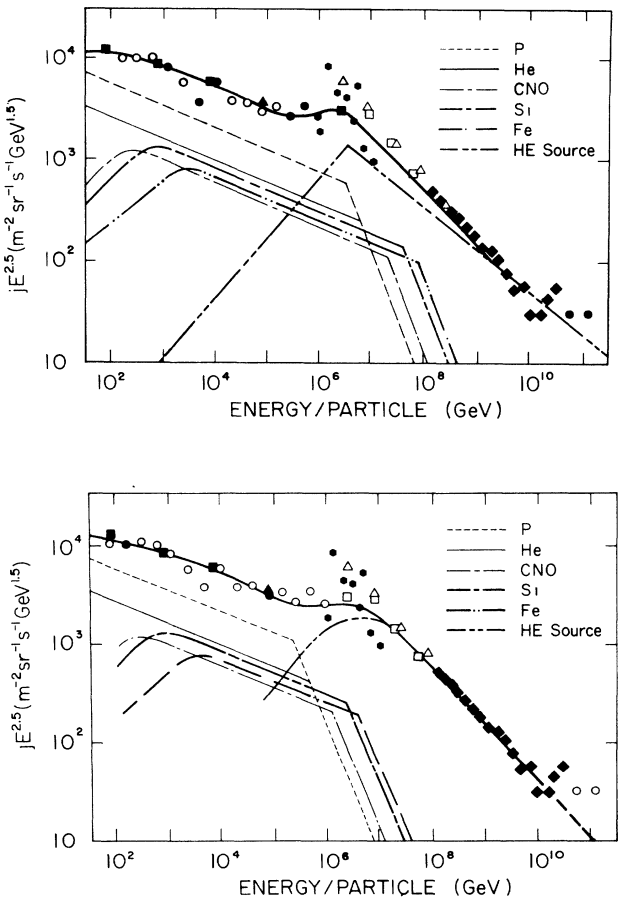

FIG. 9. Fichtel and Linsley (Ref. 26) two-source spectra. Top: "high-energy" (HE) source distributed through the galactic plane. Bottom: "high-energy" source near galactic center.

$$a = 14.5(A^{1/3}+1.32)^2 ,$$

$$b = 31.4(1.25+0.77A^{0.64}) ,$$

$$f(E) = 25.7+0.26\ln\frac{E}{M}+43.7E^{-0.436}-25.8E^{-0.575}$$

[where M=nucleon mass, E=nucleon laboratory energy (TeV), and A=atomic mass]. For the Md0 model all nucleons interact like free nucleons, independent of the nuclear binding.

The inelastic cross section for nucleon-air collisions are computed from

$$\sigma^{\text{inel}}_{N\text{-air}} = 260+11\ln(10E) .$$

For mesons

$$\sigma^{\text{inel}}_{\pi\text{-air}} = \sigma^{\text{inel}}_{K\text{-air}} = 0.72\times\sigma^{\text{inel}}_{N\text{-air}} .$$

(ii) Nuclear fragmentation. A projectile nucleus fragments according to the probabilities compiled by Wlodarczyk *et al.*[30] for all models but Md0. For the Md0 model, a projectile nucleus is assumed to be a superposition of nucleons all of equal energy, each interacting independently.

(iii) Leading-particle distributions. The longitudinal momentum of the leading particle is chosen differently in different models. The Md0 and Md1 models produce a uniform distribution in Feynman x for nucleons ($\bar{x}=0.5$) and a step in the distribution of Feynman x for mesons ($\bar{x}=0.28$). Md2 is a high-inelasticity model producing an average Feynman x of $\bar{x}=0.31$ for nucleons.

(iv) Secondary-particle type. Each secondary particle is randomly assigned to be a nucleon, kaon, or pion.

In the Maryland models the probability to produce a nucleon is

$$P(N) = 0.0164\ln(1+0.015E) \quad \text{for incident nucleons} ,$$

$$P(N) = 0.0028\ln(1+0.015E) \quad \text{for incident mesons} ,$$

where E is in GeV.

In these models a secondary not assigned to be a nucleon is chosen to be a kaon with probability 0.1, and is otherwise a pion. Pions are neutral with probability $\frac{1}{3}$ and kaons with probability $\frac{1}{2}$.

In the SHOWERSIM models, the assignment of particle identity has different energy dependence than in the Maryland models and reflects more current results from the CERN SPS. Below 1-TeV (laboratory frame) incident energy, kaons, and pions are produced in the ratio 1:9, as in the Maryland models, but no nucleons are produced. Above 1 TeV, the A00 model produces nucleons and η mesons.[28] F00 and F2 have no nucleon production.

(v) Inclusive x distributions. The longitudinal momenta of secondary particles are chosen from the distributions

$$\frac{dN}{dx} \propto \frac{1}{x_r}e^{-\alpha x} ,$$

E^* is the secondary energy and $\sqrt{s}$ is the total energy, both in the barycentric system. α is chosen according to the values shown in Table II. Where two entries are shown, one or the other is chosen by the simulation with equal probability.

(vi) Transverse-momentum distributions. The transverse-momentum distribution for all hadrons in the Maryland models and all secondaries (excluding the leading particle) in the SHOWERSIM models is taken to be

$$\frac{dN}{dP_t} \propto P_t\left[1-\frac{P_t^2}{w}\right]^{-4} , \quad w = a+b\ln\sqrt{s} ,$$

$$a = 5.52\times10^{-4}, \quad b = 26\times10^{-6} \quad \text{for } \pi ,$$

$$b = 30\times10^{-6} \quad \text{for } K, \quad b = 26\times10^{-6} \quad \text{for nucleon} .$$

The azimuthal angles of secondary particles are chosen at random. Approximate transverse-momentum balance is thereby obtained.

(vii) Electromagnetic component. Electromagnetic showers are initiated from photons emitted in the decay of π^0's or η^0's. The ensuing electromagnetic shower produces particles which are followed until their energy falls

TABLE II. Values of α for Maryland models.

Secondary type	Nucleon collisions	Pion collisions
Nucleon	11	2.5
Meson	5.5 or 6.5	3.4 or 3.5

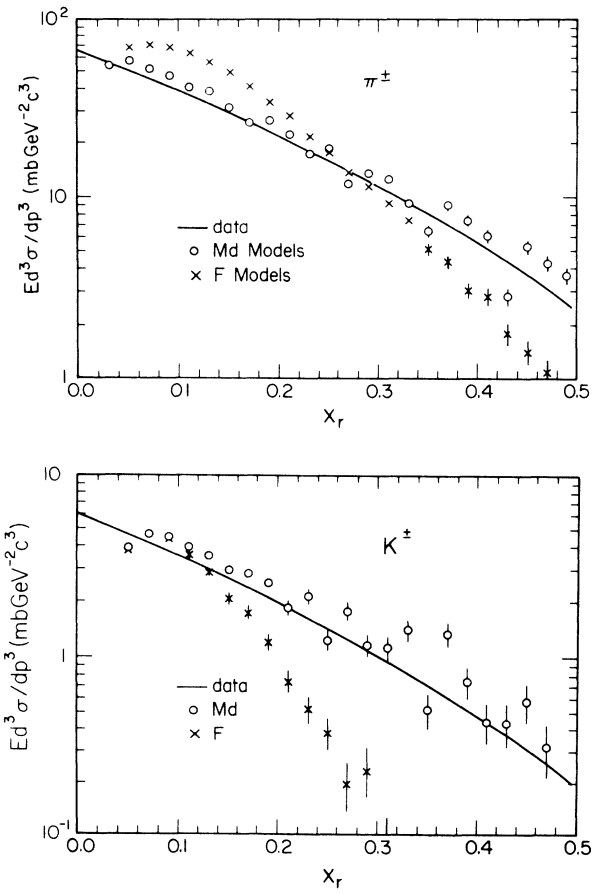

FIG. 10. Invariant cross section for $\pi^{\pm}$ (top) and $K^{\pm}$ (bottom) production vs x_R for p-p collisions at $\sqrt{s}=27.4$ GeV. $p_t=0.2$–0.3 GeV/c.

below 200 GeV. The further shower development is treated analytically with Approximation B (Ref. 31). The shower age is computed and the lateral shower density at the depth of the detector is calculated from the distribution of Nishimura, Kamata, and Greisen[32] as modified by Hillas and Lapikens.[33]

(viii) Comparisons of models with accelerator data. The prediction of the interaction models were compared with results from accelerator experiments. The dependence of the simulated invariant cross section on radial x is compared with experimental data from Fermilab (Ref. 28) at $\sqrt{s}=27.4$ GeV in Fig. 10. The agreement with data for pions is very good for the Maryland models with differences for the SHOWERISM models. As the energy is increased the predicted radial x distribution for the two types of models merge (Fig. 11).

The cross section for all changed hadrons at $\sqrt{s}=540$ GeV is shown as a function of transverse momentum[34] in Fig. 12. The agreement between the Monte Carlo results and data is very good at small transverse momenta where the cross section is large.

The average multiplicities for the different models are compared in Table III with data at various energies.

TABLE III. Particle multiplicities compared to data.

h	$\pi^{\pm}$	π^0	$K^{\pm}$	$p,\bar{p}$	η^0	$h^{\pm}$
			$\sqrt{s}=45$ GeV			
Data	8.67	4.7	0.80	0.56	0	$10.03\pm\approx 10\%$
Md1	9.26	4.58	0.76	0.86	0	11.88±0.16
A00	7.07	3.55	0.60	0.50	0.01	8.22±0.17
F00	7.90	3.83	0.70	0	0	9.1±0.18
F2	10.81	5.46	0.87	0	0	12.6±0.2
Md2	12.68	6.39	1.10	1.98	0	15.8±0.7
			$\sqrt{s}=53$ GeV			
Data	9.0	4.2	0.75	0.30	1.1	10.1
Md1	11.8	6.0	0.94	1.13	0	14.5±0.2
A00	8.35	4.2	0.74	0.06	0.19	9.6±0.2
F00	9.7	5.2	0.80	0	0	11.0±0.2
F2	13.2	6.7	1.10	0	0	14.8±0.2
Md2	15.7	7.8	1.22	1.89	0	18.9±0.2
			$\sqrt{s}=540$ GeV			
Data	22.3	10.1	2.5	1.5	3.5	26.5
Md1	32.2	15.8	2.27	3.6	0	39.8±0.3
A00	20.2	9.9	2.0	1.08	3.3	24.6±0.2
F00	23.1	16.3	2.2	0	0	26.82±0.25
F2	31.7	22.5	3.2	0	0	37.0±0.2
Md2	43.8	21.7	3.3	5.8	0	54.1±0.2

D. Simulation of detector response

The general scheme for determining the probability of an air-shower triggering the experiment was described in Sec. IV A. The process of sweeping the simulated detector over the entire grid minimizes computer time. Although no one hadron is sampled more than once, the samples are not statistically independent. A probability is computed for triggering for each primary species and energy interval.

In order to simulate the signals observed, the response of the calorimeter to single hadrons must be known. To this end, a prototype of the calorimeters was taken to the Alternating Gradient Synchrotron at Brookhaven, where it was calibrated in a test beam up to 10 GeV/c (Ref. 35).

For hadrons with momentum less than 10 GeV/c, the signal distribution used in the simulation is drawn directly from the measured data. Above 10 GeV/c the response was simulated using the CALORS (Ref. 36) code developed at Oak Ridge National Laboratory. The code produced excellent agreement with both the Brookhaven data and data at energies of 50, 100, and 278 GeV from another experiment with a similar calorimeter configuration.[36] The simulations were also used to reproduce the lateral spread of signals. This allowed for calculation of both signal sharing between quadrants and for the addition of signals which come from hadrons interacting in the shielding surrounding the calorimeter.

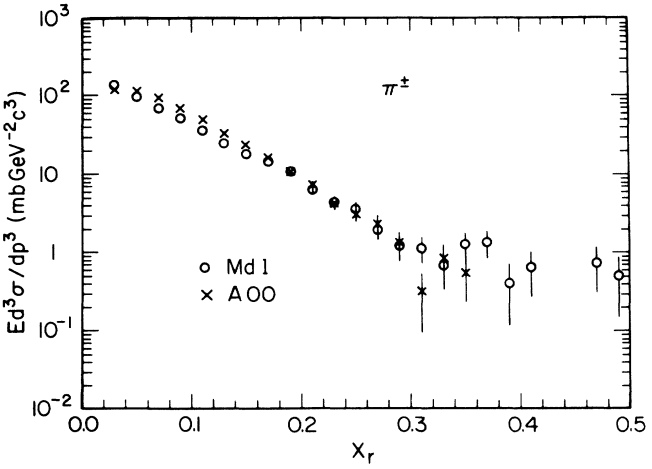

FIG. 11. Invariant cross section for $\pi^{\pm}$ vs x_r for p-$\bar{p}$ collisions at $\sqrt{s}=540$ GeV. $p_t=0.2$–0.3 GeV/c.

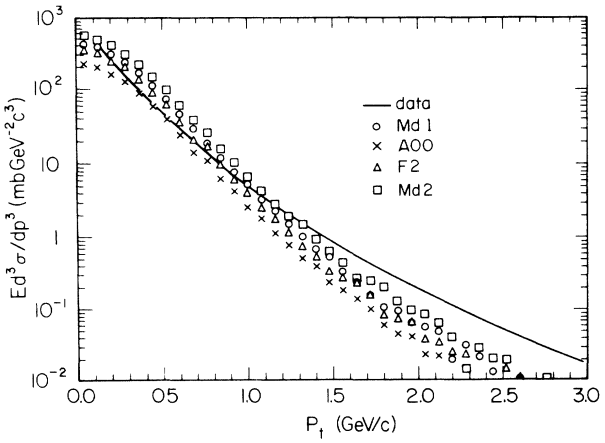

FIG. 12. Invariant cross section vs p_t for all $h^{\pm}$ for p-$\bar{p}$ collisions at $\sqrt{s}=540$ GeV, $y=2.5$.

The arrival time of each hadron was calculated by the air-shower simulation. The measured probability of firing a TDC as a function of signal was used to determine whether a hadron stopped the TDC. The time of the first arriving hadron which stopped the TDC was stored in the grid cell. Fluctuations consistent with the resolution were included. If a signal arrived early and was large enough to exceed the TDC threshold all timing information about successive hadrons was lost, just as in the actual experiment.

The calorimeter response to included hadrons was estimated by using the ratio between average B and C counters for the depth dependence of the shower and then correcting the signal by the secant of the incidence angle.

Several other processes give rise to signals in the calorimeters and were simulated. In dense air showers, electrons passed through the light pipes of the B and C counters. These produced Cherenkov light which added signal to the counters and, if large enough, may have produced a prompt TDC signal "vetoing" any later arriving hadrons. The effect of the Cherenkov light was measured by removing the scintillator and recording the signal and fraction of TDC triggers as a function of shower density. Data from this test were incorporated into the simulation. Thus, signals not originating in the scintillators were accounted for.

Muons accompanying the air shower passed through the detector and some fraction of them produced signals large enough to stop the TDC. Even those which did not stop the TDC added signal to the ADC. In order to simulate the effects of these muons, a modified version of the air-shower simulation was run. Muons with energy as low as 2 GeV were followed through the atmosphere to the detector level. The simulation program calculated lateral position, arrival time, and total number of muons for various primary particles. The results were fitted to functional forms and incorporated into the GRID simulation. In GRID, the probability of finding a muon in a particular quadrant was calculated. If a muon was present, its arrival time was picked from the simulated probability distribution. The amplitude of the counter signal was selected from a measured distribution of counter response to muons and added to any other signals present as in the actual experiment. The probability that the TDC fired because of a muon, was measured as a function of the muon signal size and was also incorporated in the simulation.

The shower density simulated at each calorimeter was used to calculate the average number of shower particles passing through the A counters. The measured shower density was simulated from a Poisson probability distribution whose mean was the average number of shower particles computed above. Particles backscattering to the A counters from hadronic showers in the calorimeter were measured by comparing the signals in a counter on the calorimeter with those of an identical counter adjacent to the calorimeter. The results were found consistent with the simulated A counter signal from a simulation of backscattering with the program CALOR. The backscattered particles were added to the shower-density detector simulation.

The experimental off-line cuts were applied to the simulated data in the grid cells to determine event triggering efficiency as a function of primary type and energy. The trigger rate for a particular primary was obtained by multiplying the triggering efficiency by the area, the solid angle, the exposure factor, and the primary flux in the appropriate energy interval. All species and spectra were combined together. The resulting rates were compared with the data. In Sec. V the trigger rate and the primary spectrum are discussed. The delayed spectrum is treated in Sec. VI and various other measured parameters are compared with simulations in Sec. VII.

V. THE PRIMARY SPECTRUM FROM TRIGGER RATE AND ALL-PARTICLE MEASUREMENTS

A. Comparison with all-particle flux measurements

The different primary spectral models discussed in Sec. IV B are compared with measurements of the all-particle flux. The trigger rates that these models predict for each of the interaction models (Sec. IV C) are compared with the measured rate. Primary spectra enriched in heavy nuclei fit the measurements better than proton-dominated spectra.

The measurements of the all-particle flux come from two sources. The highest-energy direct measurements are those of Grigorov *et al.*[10] At energies above those where direct measurements exist, it is necessary to use determinations of the flux from extensive-air-shower (EAS) measurements. The points of Khristiansen,[37] were chosen because they agree fairly well with Grigorov at 10^{15} eV, an energy at which EAS data is scarce.

Fifteen of the Grigorov points are included in the data set. The first 11 points are a good fit to a power law.[3] Let $(J>E)$ be the integral flux above energy E. Then

$$\ln J(>E)=(43.1\pm0.3)-(1.63\pm0.01)\ln E \ ,$$

$$8.6\times10^{11}<E_{(\mathrm{eV})}<10^{5} \ .$$

Three other points within this energy range, which had been given large systematic error bars by the authors, were discarded for being more than two standard deviations from the fit. The remaining points were not furnished with error bars, so the variance of their fit was taken as the standard deviation. The Khristiansen[37] points were presented with error bars.

The quantity minimized in the fits to these points is the χ^2 per point:

$$\chi^2=\frac{1}{24}\sum_{i=1}^{24}\frac{[J(>x_i)-y_i]^2}{\sigma_i^2} \ ,$$

where y_i is the integral flux of Grigorov or Khristiansen at energy x_i and $J(>x_i)$ is the flux calculated from one of the four spectral types. The χ^2 defined here does not behave statistically as usual since errors in the integral plot points are correlated and there are various systematics that have not been taken into account. Nonetheless, it

can be used as a goodness-of-fit criterion to the extent of identifying those spectra which fit and those which do not fit the all-particle spectrum. A summary of the information on the primary flux provided by the χ^2 test is given by Fig. 13. Contours of constant χ^2 are drawn on the E_c vs γ plane (see Sec. IV B). The small open circles denote the absolute minimum.

The scatter of points in the region of $10^{15}-10^{16}$ eV precludes a χ^2 of less than 2.0 for any spectrum not tailored to fit these data (see Figs. 7 and 8). The scatter of points in this energy range also makes the value of χ^2 more sensitive to γ than to E_c as may be observed in the contour plots.

B. Trigger rate from primary spectra

The trigger rate for a given primary spectrum and particle-interaction model is calculated from the product of the flux incident upon the atmosphere (particles/m^2 sr sec) per unit of primary energy,

$$\frac{dn_A(E)}{dE}$$

for each elemental species A, the simulated number of triggers per shower, the detector area, and the detector solid angle. The number of triggers per shower, $\epsilon_A(E)$, is the number of triggers a single hadron would initiate in an infinite grid of nonoverlapping detectors of area S and solid angle Ω. $\epsilon_A(E)$, is shown in Fig. 14 for one interaction model, Md1. The area-solid angle

$$(S\Omega)=\int_{\text{grid cell}}\cos\theta\, dS\, d\Omega\ .$$

In this experiment

$$0\le\theta\le\frac{\pi}{4},\quad (S\Omega)=\frac{\pi}{2}S\ .$$

The trigger rate is given by

$$N=\frac{\pi}{2}S\sum_A\int\frac{dn_A(E)}{dE}\epsilon_A(E)dE\ ,$$

where S is the area of all four of the calorimeters (5.95 m^2).

In Fig. 13 the spectra which best match the trigger rates are drawn as a band over the χ^2 contours of the fit to the all-particle spectrum. These plots show the com-

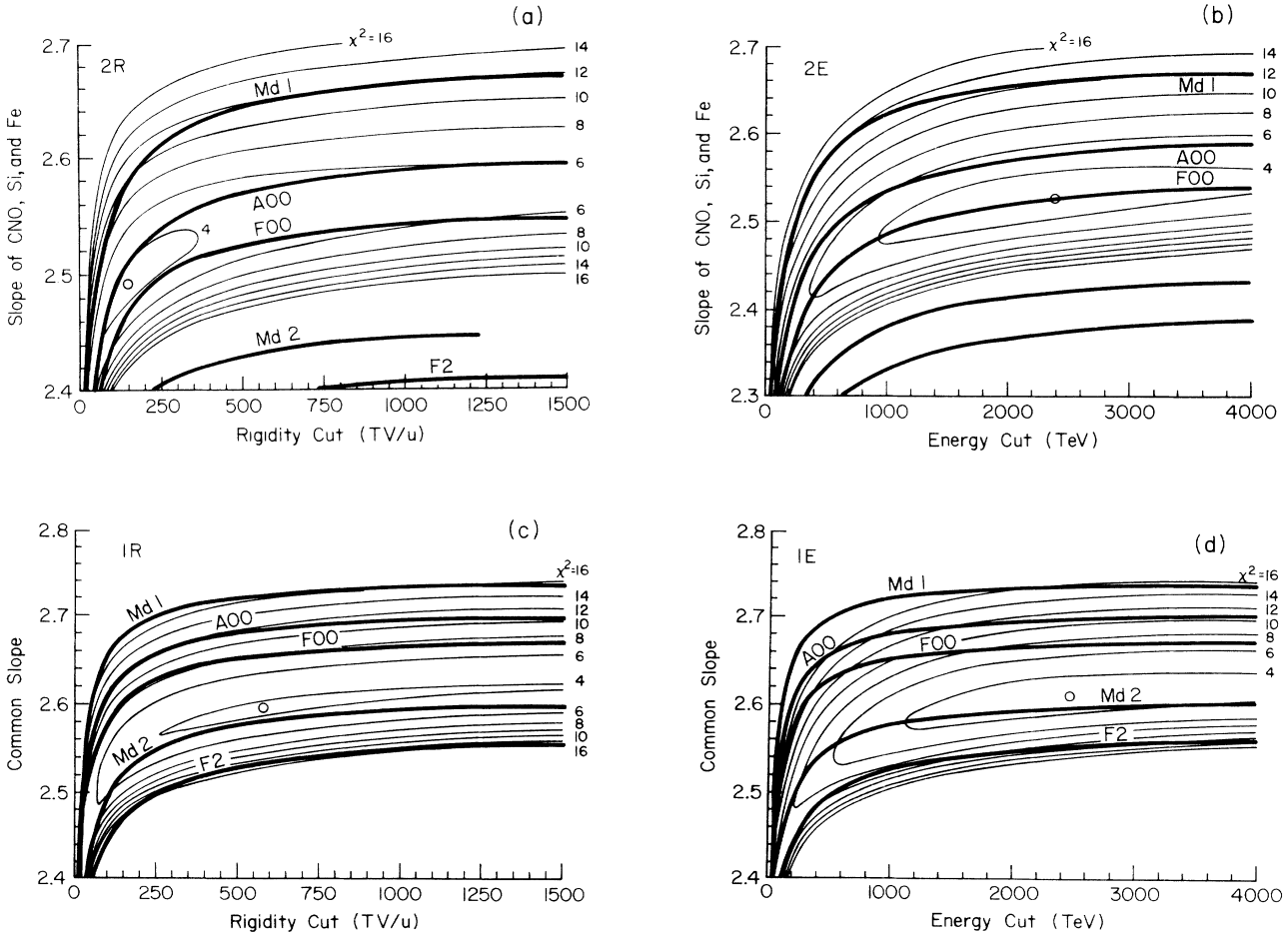

FIG. 13. The contours are loci of constant χ^2 of the fit to the all-particle spectrum from Grigorov *et al.* and Khristiansen *et al.* for (a) 2R spectra, (b) 2E spectra, (c) 1R spectra, and (d) 1E spectra. Contours start at $\chi^2=4$ and differ by 2. The small open circles denote the absolute minimum. The heavy bands match the measured trigger rate of 3.78/h for the interaction models indicated.

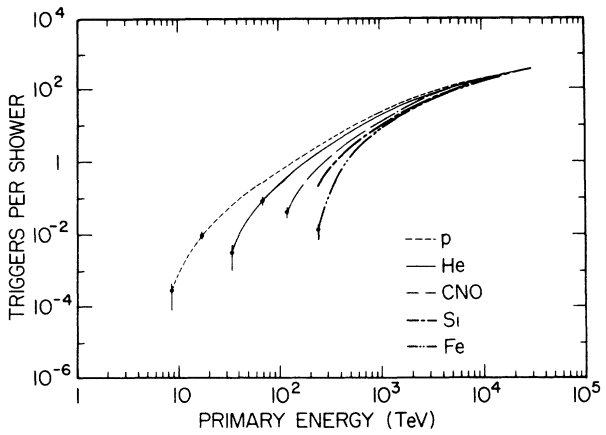

FIG. 14. Triggers per shower for Md1 model. $\epsilon_A(E)$ as a function of primary energy.

binations of (E_c,γ) that best fit the trigger rate for each spectral type and the goodness of their fits to the data of Grigorov *et al.* and Khristiansen *et al.*

The interaction models believed most realistic, A00, F00, and Md1, can match the trigger rate for all four spectral models, but the χ^2 of the matching spectra are unreasonably large for the 1E and 1R models. Only types 2R and 2E are simultaneously compatible with the trigger rate measured in this experiment, data from accelerators, and data on the all-particle integral flux. One-slope models 1R and 1E, which agree with the all-particle spectrum, predict a trigger rate too high to match our data. For the 1R model the point of minimum χ^2 (571,2.58), yields a trigger rate of 6.77/h for Md1 and a rate of 5.71/h for A00. For 1E, the corresponding rates are 6.69/h and 5.70/h. These should be compared with the measured trigger rate of 3.78±0.05/h.

The one-slope spectra, which are all proton rich, require high inelasticity models, Md2 and F2, to reduce the triggering probability sufficiently to agree with our data and the all-particle spectrum. The high inelasticity interactions cause the proton showers to attenuate rapidly thus reducing the trigger rate. Md2 and F2 are incompatible with the two-slope spectra because they yield too low a trigger rate for parameters matching the all-particle spectrum.

Table IV lists the spectral parameters obtained through two methods: (1) the trigger rate and the all-particle spectrum (Sec. V) and (2) the trigger rate and the rate of delayed hadrons (Sec. VI). Listed for the method involving the all-particle spectrum are the parameters minimizing χ^2 for each model of spectrum. The maximum χ^2 considered was 12.0. Each combination of spectrum and interaction model listed yields a trigger rate of (3.783–3.786)/h and a delayed rate of (0.046–0.054)/h.

The trigger rates with the fifth spectral model, the two source spectra of Fichtel and Linsley,[26] are shown in Table V. The spectra of Fichtel and Linsley were designed to fit the all-particle data, and so no attempt was made to improve them by fitting to those data. Like the one-slope models (1R and 1E), the proton-dominated model of Fichtel and Linsley exceeds the measured trigger rate (3.78±0.05) unless used in conjunction with an extreme model of high-energy interactions such as

TABLE IV. Best-fitting spectra matching trigger rate.

Spectrum	Model	χ^2	E_c Trigger rate and all-particle spectrum	γ	E_c Trigger rate and delay rate	γ
2R	Md0				80–300 TV/u	2.50–2.65
	Md1	5.6	59.5 TV/u	2.50		
	A00	3.7	135 TV/u	2.50		
	F00	4.2	265 TV/u	2.50		
	Md2	>43				
	F2	>106				
2E	Md0				200–400 TeV	2.4–2.5
	Md1	>12				
	A00	3.6	1100 TeV	2.54		
	F00	3.1	2200 TeV	2.52		
	Md2	>28				
	F2	>85				
1R	Md0				5×10^4 TV/u	2.8
	Md1	>15				
	A00	11.3	91 TV/u	2.60		
	F00	8.3	142 TV/u	2.60		
	Md2	4.2	571 TV/u	2.58		
	F2	>13				
1E	Md0				5×10^5 TeV	2.8
	Md1	>15				

TABLE V. Trigger rates (per hour) from the Fichtel-Linsley spectra. S_1 is the contribution to the rate from the "low-energy" source and S_2 is the contribution from the "high-energy" source.

Model	S_1	S_2	Full rate
	(1) R Cut=3000 TV/u		
Md1	4.33	0.94	5.27
A00	3.16	1.90	5.06
F00	3.78	1.34	5.12
F2	2.17	1.08	3.25
Md2	2.81	1.22	4.03
	(2) R Cut=500.5000 TV/u		
Md1	4.03	1.11	5.14
A00	3.89	2.20	6.09
F00	3.29	1.53	4.82
F2	1.75	1.25	3.00
Md2	2.17	1.39	3.56

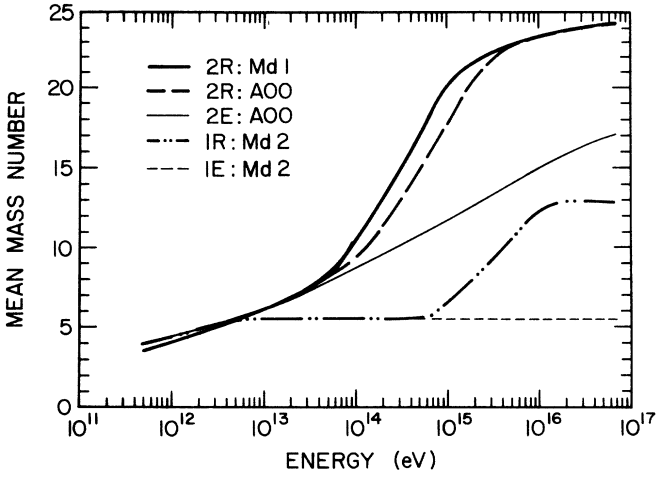

FIG. 16. Geometric mean of the mass number vs energy.

Md2 and F2.

The range of energies over which this experiment is sensitive is indicated in Fig. 15. The trigger rate is plotted as a function of primary energy for the best-fitting models, interaction model A00 and spectral model 2R near the minimum χ^2 matching the trigger rate. The geometric mean of the mass of the primary flux is shown as a function of energy in Fig. 16 for the best fitting spectra matching the trigger rate for each of the interaction models. At 1000-GeV primary energy, the two-slope models favor a heavy composition while the one-slope models favor a lighter composition. A light composition requires the F2 or Md2 interaction models. Both these interaction models make the extreme assumption that the inelasticity is substantially larger than observed at accelerator or collider energies.

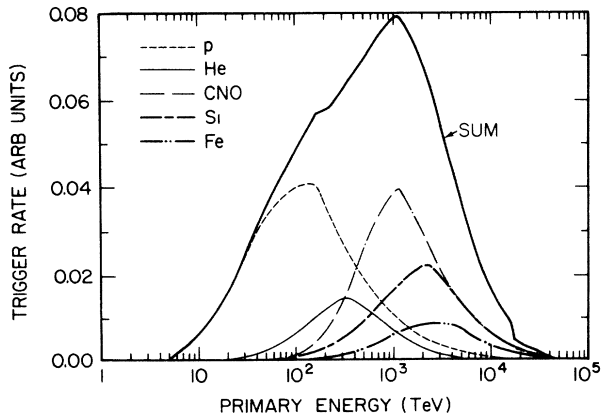

FIG. 15. Trigger rate vs primary energy. Interaction model A00 and 2R spectrum. Rigidity cut =166 TV/u. Spectral indices: $\gamma_p=\gamma_{He}=2.78$, $\gamma_{CNO}=\gamma_{Si}=\gamma_{Fe}=2.51$.

VI. SPECTRUM FROM TRIGGER AND DELAY RATES

In Sec. V the rate of triggers was combined with information on the all-particle spectrum to determine the elemental composition as a function of energy. The only trigger characteristics used were the total hadronic energy measured and the local shower density, those quantities needed to define a trigger. In this section, a second method is described to distinguish between models of the primary spectrum. The rate of triggers is combined with the rate of arrival of hadrons delayed with respect to the shower front to obtain constraints on the four composition models: 2R, 2E, 1R, and 1E. The results of the two methods of determining γ and E_c are compared.

The simulation of the delays was done using particle-interaction model Md0. In the simulation, delayed hadrons were found to come mainly from low-energy nucleons lagging behind the shower front. These nucleons were from three sources in nearly equal proportion: (1) nucleons from the primary cosmic ray propagated through the atmosphere to the detector, (2) target nucleons ejected by the interactions in the shower development, and (3) nucleon-antinucleon pairs created in the interactions. Heavy primary nuclei produce more delayed hadrons than primary protons. Models with less nucleon production than model Md0 will predict lower delayed rates and therefore will require primary spectra with a greater fraction of heavy nuclei.

The pulse-height distribution of delayed events is compared with that predicted from proton and iron primaries in Fig. 17. Both proton and iron primaries give a distribution consistent with the data. Any mixture of them is also consistent with the data; the pulse-height distribution of delayed events is therefore insensitive to composition. The distribution is, however, sensitive to the response of the calorimeter to hadrons. Although the energy spectrum of delayed particles is dominated by low-energy particles the pulse-height distribution shows a long tail of large signals. The tail is a manifestation of the response function of the calorimeters to low-energy

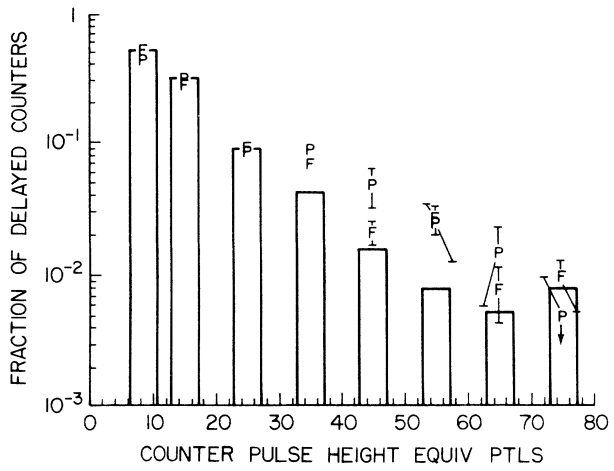

FIG. 17. The pulse-height distribution of hadrons with signal greater than seven equivalent particles and time delay greater than 20 ns. Columns are data, (*P*) are simulated events produced by protons, and (*F*) are simulated events produced by iron nuclei.

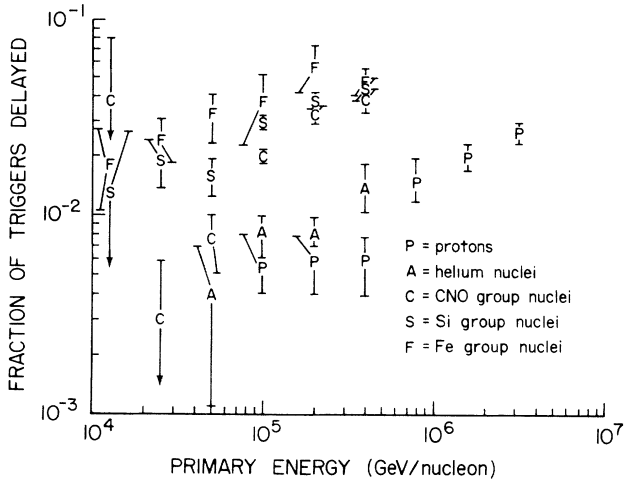

FIG. 18. Fractions of simulated triggers with signal greater than seven equivalent particles and with a delay greater than 20 ns as a function of primary energy and atomic mass. The uncertainties in the points are obtained by repeated simulations.

particles. The consistency of the large signal delays in the simulations with those in the data has been described elsewhere[1] and is an illustration of the importance of detailed detector response simulation. It should also be noted that any alternative explanation for delayed events (such as very-low-energy neutrons, which have been calculated to contribute less than 1% of the delays) would have to explain the measured pulse-height spectrum.

The fraction of simulated events with delayed hadrons is plotted as a function of primary energy and atomic mass in Fig. 18. To predict the rate of delayed events for any of the composition models, the energy distribution of delayed events was folded in with the flux predicted by the model. The normalizations used are given in Sec. IV B (Ref. 1). For the 1E and 1R models the spectral indices for proton, helium, and CNO group are taken to be $\gamma_p = 2.75$, $\gamma_{\mathrm{He}} = 2.78$, and $\gamma_{\mathrm{CNO}} = 2.6$, respectively.

The trigger rate and the delayed hadron rate were computed with each of four composition models. The results are illustrated in Figs. 19 and 20. The data are shown as a cross in the center of the diagram, with the vertical and horizontal bars of one standard deviation width of the measured delay and trigger rates, respectively. The standard deviations are statistical; no systematic uncertainties are included. The contour lines are the predictions of the model. Each curve is for a fixed spectral index, γ, at low energy. Along the curve, the delay and trigger rates increase as the rigidity or energy cut E_c increases. The measured trigger and delay rates are consistent with a range of values of E_c and γ for each of the composition models. These are shown in Table IV and can be compared favorably with the results obtained from the trigger rate and the all-particle spectrum.

Of the four models discussed, the 2R model best fits the combination of the trigger rate, the delayed rate, and the all-particle spectrum.

As noted in the conclusion of Sec. V, a proton-dominated composition such as 1R or 1E would result in about twice the number of observed triggers with interaction model Md1 (or the similar model Md0). Also, a proton-dominated composition would result in about half the number of delayed triggers. Such a model cannot therefore fit the combination of trigger and delay rates. A proton-rich composition can fit the trigger rate, but only when used with particle-interaction model Md2 or F2, which do not agree well with accelerator data. The delayed rate using model Md2 has not been calculated.

VII. STUDY OF OTHER MEASURED PARAMETERS

The five particle-interaction models and six models of primary composition were compared above for predictions of trigger rate and delayed rate and for agreement with measurements of the all-particle spectrum. Other trigger characteristics have been examined. Unlike the trigger and delayed rates, they were found to be relatively insensitive to primary composition.

(a) Shower-density distribution. The shower-density distribution of events is found to be insensitive to the composition of the primary spectrum. All of the combinations of interaction model and primary spectrum lead to density histograms in good agreement with the data up to densities of approximately 150 $e^{\pm}/\mathrm{m}^2$ (Fig. 21). All models predict too many events with shower densities greater than $150/\mathrm{m}^2$ which account for about 15% of the simulated triggers. This discrepancy may be due to the saturation of the *A* counters, not included in the simulation.

(b) Calorimeter signal distributions. The measured calorimeter quadrant pulse-height distribution is compared with the data in Fig. 22. There is little difference between the different simulated models. All models are in good agreement with data up to 300 equivalent parti-

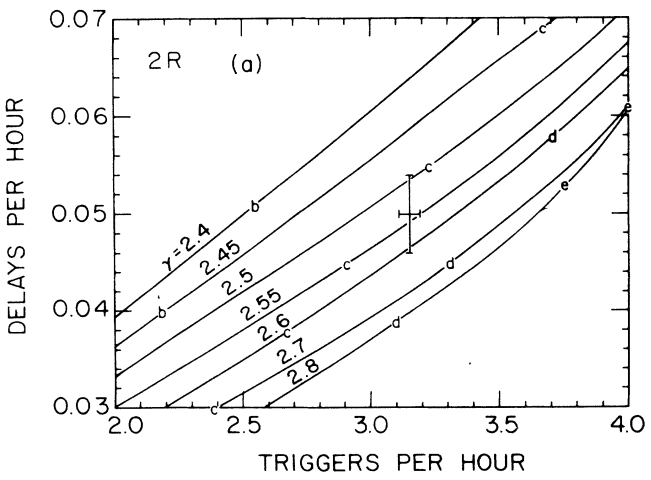

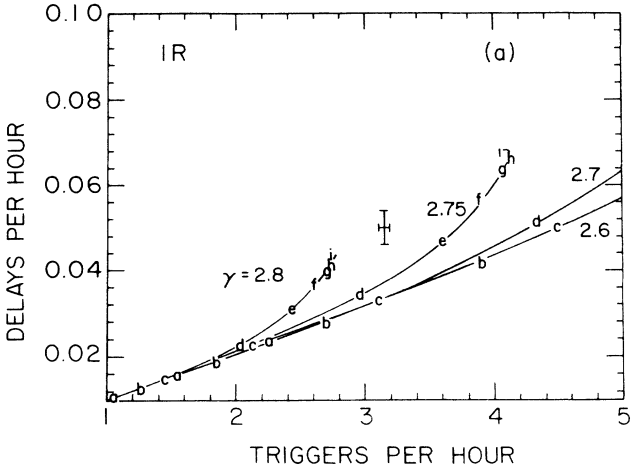

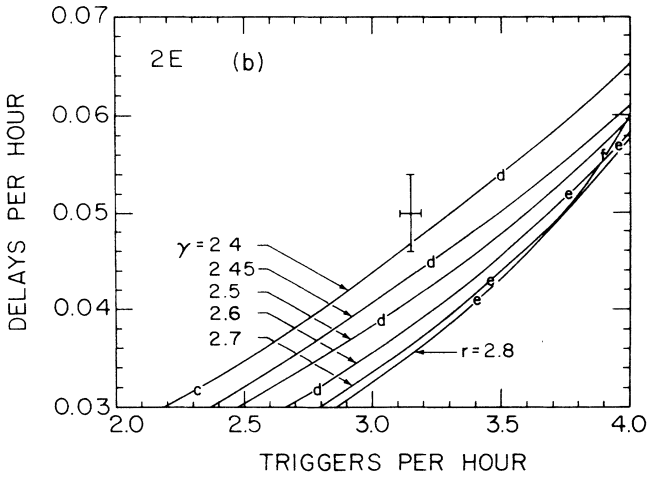

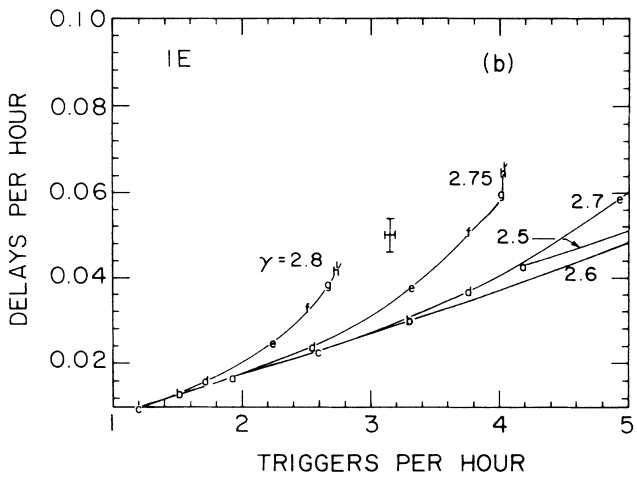

FIG. 19. Simulated trigger and delay rate for (a) composition model 2R and (b) composition model 2E. The trigger vs delay rate is for a primary spectrum with differential spectral indices $\gamma_p=2.75$, $\gamma_{He}=2.78$, and $\gamma_{CNO}=2.6$ for protons, helium, and CNO group, respectively; Fe and Si are assigned a common index which is fixed for each contour line. The contours are labeled by the index at low rigidity (energy). The spectral index steepens by 0.5 at a rigidity which varies along the contour lines. The symbols *c*, *d*, *e*, and *f*, signify rigidity (energy) cuts of 1×10^5, 3×10^5, 1×10^6, and 3×10^6 GeV, respectively, where the steepening takes place. The measured trigger and delayed rates are indicated by a cross at the center of the diagram.

FIG. 20. Simulated trigger and delay rate for (a) composition model 1R (rigidity) and (b) composition model 1E (energy). The trigger vs delay rate is for a primary spectrum with a common index for all species. The index steepens by 0.5 at a fixed rigidity (energy). The contours are labeled by the index at low rigidity (energy). The bend rigidity (energy) varies along the line. The symbols *a*, *b*, *c*, *d*, *e*, *f*, *g*, *h*, and *i* signify rigidity (energy) cuts of 1×10^4, 3×10^4, 1×10^5, 3×10^5, 1×10^6, 3×10^6, 1×10^7, 3×10^7, and 1×10^8 GeV, respectively, where the steepening takes place. The measured value is indicated by a cross at the center of the diagram.

cles. The distribution shapes are not compared above this value since the calorimeter counters are not linear for such large signals. The total number of events above this cut can be compared. Approximately 15% of simulated events contain very large pulse heights as compared with only a few percent in data.

Shower-density and calorimeter pulse-height spectra are insensitive to primary composition. Simulations demonstrated the converse was also true: raising the shower density and particle sum cuts, independently or together, did not change the proportion of the different species contributing to triggers. The only effect was to raise the average energy of particles contributing to the trigger rate for all species.

(c) Spread of hadronic energy. The spread of hadronic energy in the calorimeters could depend on the energy or on the mass of the incident primary. The higher the energy or the higher the atomic mass of the primary, the further the showers can trigger from the core. The energy-weighted center of an event is located at point (x_0,y_0), where

$$(x_0,y_0)=\frac{\left[\sum_{i=1}^{4} S_i x_i,\ \sum_{i=1}^{4} S_i y_i\right]}{\sum_{i=1}^{4} S_i}\ .$$

The ith calorimeter has a total $B+C$ signal S_i located at point (x_i,y_i). The root-mean-square spread about this point is defined as

$$\xi=\left[\sum_{i=1}^{4}\frac{[(x_i-x_0)^2+(y_i-y_0)^2]S_i}{\sum_{i=1}^{4}S_i}\right]^{1/2}.$$

In order to decrease the sensitivity of this parameter to very low-pulse heights, a ten equivalent particle cut was placed on each summed calorimeter pulse height. The predicted and measured rms values are compared in Fig. 23. The rms distribution is very similar for all interaction models and primary spectra. The Monte Carlo events are deficient in spreads of more than two meters, indicating that a larger fraction of the real events have nonzero signals in both calorimeters I and IV. The peaks and valley of the rms distribution are also sharper than in data because there are fewer events in which three or four calorimeters have nonzero signals.

The shower density, event, or quadrant signal and rms spread of hadronic energy are not sufficiently sensitive to interaction model or primary spectrum to be useful in this experiment. For the great majority of events, those without very large counter signals or shower densities $>150/\mathrm{m}^2$, there is good agreement between data and the "best" combinations of spectrum and interaction model in all three areas here analyzed, leading support to the use of the trigger rate as a means of comparing Monte Carlo events to data. However, the simulated events differ from the real events in several respects: (1) they have more events with high-energy (equivalent particles) hadrons; (2) they have more events with high-shower densities ($>150/m^2$); (3) they have fewer events with a large (>2 m) spatial spread of hadronic energy.

VIII. CONCLUSIONS

The experiment was sensitive to hadrons from cosmic-ray showers with energies $10^{13}<E<10^{16}$ eV. In the energy interval covered, the index of the all-particle energy

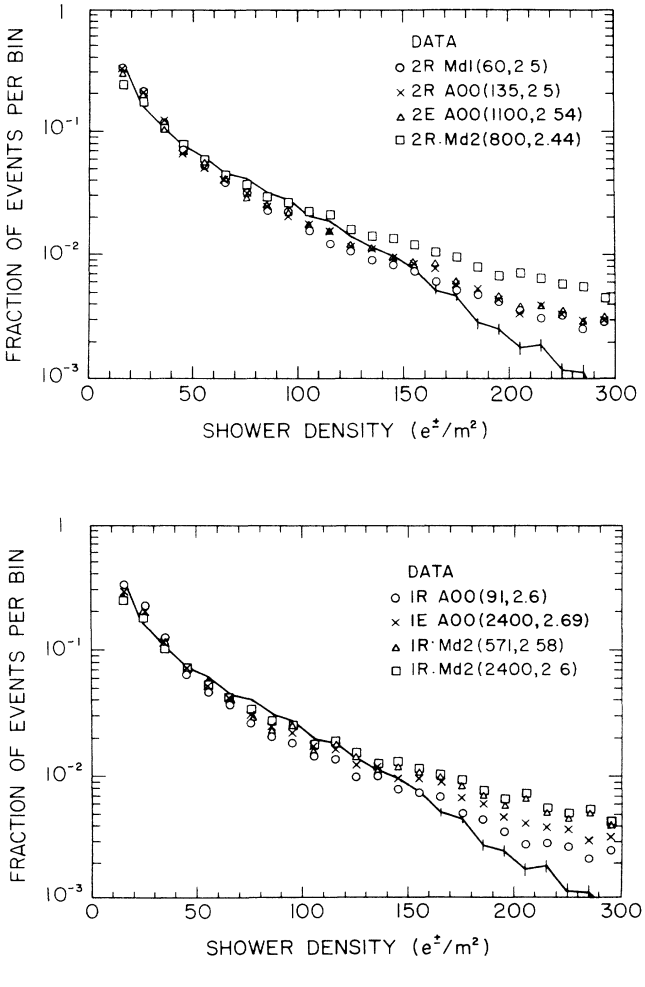

FIG. 21. Shower-density distributions measured and simulated with different combinations of interaction model and composition model. Top: two-slope spectra 2R and 2E. Bottom: one-slope spectra 1R and 1E.

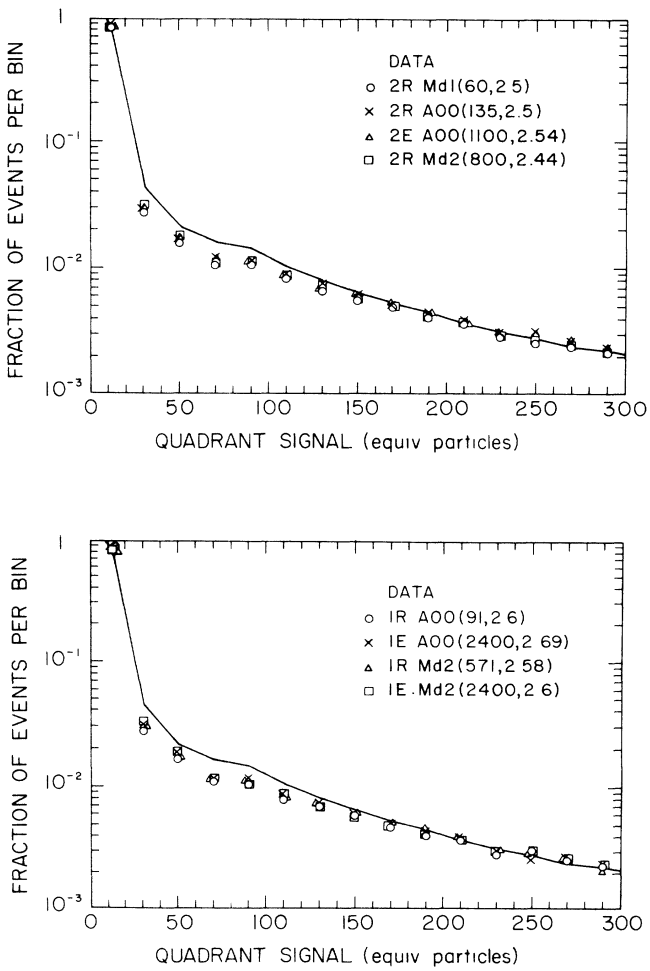

FIG. 22. Histograms of quadrant signals. Top: two slope. Bottom: one slope.

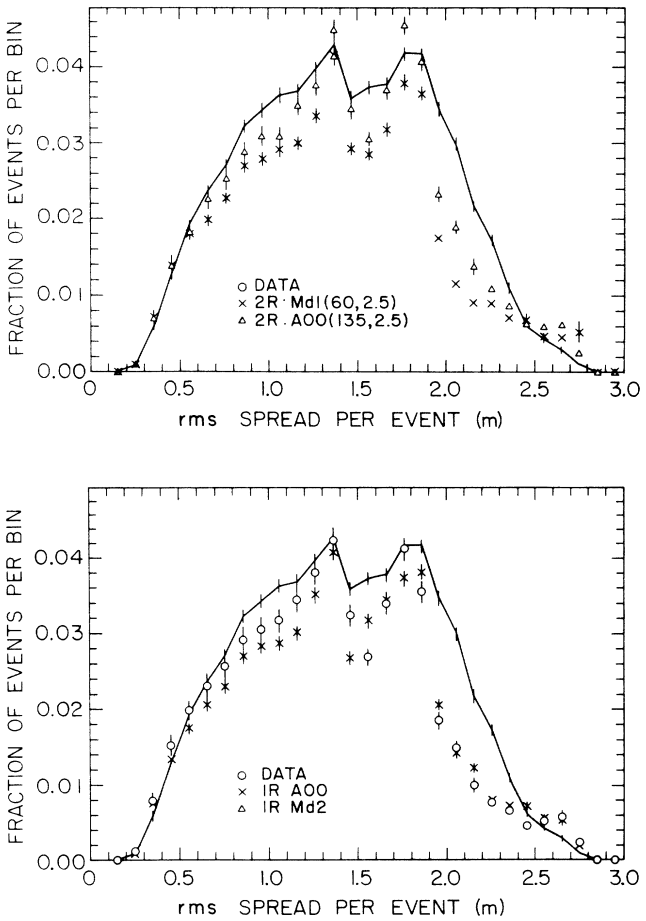

FIG. 23. Histogram of rms spread per event. Top: 2R spectrum with Md1 and A00. Bottom: 1R spectrum with Md2 and A00 (the "best" fits). Line = data. The four possible distances between calorimeters i and j are (1) $r_{12}=r_{34}=2.73$ m, (2) $r_{23}=3.45$ m, (3) $r_{12}=r_{24}=3.66$ m, (4) $r_{14}=5.46$ m. The distribution peaks at half the distance between the calorimeters. The maximum value of ξ_{ij} is $r_{14}/2=2.73$ m.

spectrum changes, the so-called "region of the bend." This range of changing spectral index is also apparently accompanied by changes in the cosmic-ray composition.

The nuclear-electromagnetic cascades induced by cosmic rays were simulated with six different models of hadronic interactions. These were convoluted with five different models of cosmic-ray composition and energy spectra. The simulations were quantitatively compared with previously reported measurements of the all-particle flux[10,37] and the measured trigger rate of this experiment. The statistic used was a weighted least squares, called χ^2 in the text. The uncertainties were not precisely known and the confidence levels were therefore not calculated.

We are confident of the following conclusions. Those compositions models which are proton-rich fit the data only if hadronic interactions were of high inelasticity, which at accelerator energies is consistent with data. The arrival-time distribution of hadrons with respect to the shower front provided an independent parameter sensitive to composition. The study of delayed hadrons was also inconsistent with a proton-dominated spectrum, in agreement with the result from the trigger rate. The data of this experiment are consistent with a substantial fraction of nuclei heavier than helium at 10^{15} eV.

Indirect measurements require care in their comparison. We have found the hadron inelasticity to be an important factor in the interpretation of the results. If hadronic interactions had a high inelasticity (0.7, for example), the data from this experiment would have indicated that the cosmic-ray spectrum composition is dominantly protons at the energies of this experiment, 10^{15} eV, as it is at lower energy, 10^{12} eV. High inelasticity is ruled out at Fermilab fixed-target energies and there is no evidence that it increases rapidly at higher energy; under these condition we would conclude that near the bend energy, heavier nuclei dominate the cosmic-ray spectrum.

ACKNOWLEDGMENTS

This work was supported in part by grants from the National Science Foundation (PHY 82-07425 and PHY 85-07637). The support from the Computer Center of the Tata Institute of Fundamental Research is gratefully acknowledged. The work of H.T.F. and A.I.M. was done in partial fulfillment of their respective Ph.D. degrees.

*Present address: ST Systems Corporation, Lanham, MD 20706.
†Present address: New York University, New York, NY 10013.
‡On leave from the National Science Foundation, Washington, DC 20550.
§Present address: Tata Institute of Fundamental Research, Bombay, India 400 005.
**Present address: University of California at Irvine, Irvine, California 92717.

[1]A. I. Mincer *et al.*, Phys. Rev. D **32**, 541 (1985); A. I. Mincer, Ph.D. thesis, Univeristy of Maryland, 1984, Report No. PP-85-18.
[2]J. A. Goodman *et al.*, Phys. Rev. Lett. **42**, 854 (1979); J. A. Goodman *et al.*, Phys. Rev. D **26**, 1043 (1982).
[3]H. T. Freudenreich, Ph.D. thesis, University of Maryland, 1986.
[4]T. H. Burnett *et al.*, Phys. Rev. Lett. **51**, 1010 (1983); T. H. Burnett *et al.*, Nucl. Instrum. Methods **A251**, 583 (1986).
[5]The spectral index of the intregral spectrum will be denoted by Γ and the spectral index of the differential spectrum will be denoted by γ.
[6]M. Ryan *et al.*, Phys. Rev. Lett. **28**, 985 (1972); **28**, 1497(E) (1972).
[7]M. Simon *et al.*, Astrophys. J. **239**, 712 (1980).
[8]T. H. Burnett *et al.*, in *Proceedings of the International Symposium on Cosmic Rays and Particle Physics*, Tokyo, Japan, 1984, edited by A. Ohsawa and T. Yuda (Institute for Cosmic Ray Research, Tokyo, 1984), p. 468.

[9]V. K. Balasubramanyan *et al.*, in *Proceedings of the International Symposium on Cosmic Ray Superhigh Energy Interactions,* Beijing, 1986, edited by Ding Lin Kai, J. Haoatruai, and Ren Jengru (Institute of High Energy Physics, Academia Sinica, 1986), p. 6-1.

[10]N. L. Grigorov *et al.*, in *Proceedings of the 12th International Cosmic Ray Conference,* Hobart, Tasmania, 1971 (University of Tasmania Press, Hobart, Tasmania, 1971), Vol. 2, p. 206.

[11]J. Grunsfeld *et al.*, Astrophys. J. **327**, L31 (1988).

[12]J. Esposito, Ph.D. thesis, University of Maryland, 1988.

[13]T. K. Gaisser *et al.*, Rev. Mod. Phys. **50**, 859 (1978); G. B. Yodh, in *Cosmology and Particles,* proceedings of the Moriond Meeting on High Energy Astrophysics, Les Arcs, France, 1981, edited by J. Audouze *et al.* (Editions Frontières, Dreux, France, 1981), p. 23.

[14]M. La Pointe *et al.*, Can. J. Phys. **46**, S86 (1968); H. Bradt *et al.*, in *Proceedings of the 9th International Cosmic Ray Conference,* edited by A. C. Strickland (Institute of Physics and Physical Society, London, 1966), Vol. 2, p. 715; A. M. Hillas, Phys. Rep. **20C**, 59 (1975).

[15]C. M. G. Lattes *et al.*, Phys. Rep. **65**, 151 (1980); M. Akashi *et al.*, Phys. Rev. D **24**, 2353 (1981); Pamir Collaboration, in *Proceedings of the Symposium on Cosmic Ray Superhigh Energy Interactions* (Ref. 9), p. 3-1; J. R. Ren *et al.*, *ibid.*, p. 3-24.

[16]G. B. Khristiansen *et al.*, in *Proceedings of the 12th International Cosmic Ray Conference* (Ref. 10), Vol. 6, p. 2097; N. N. Kalmykov *et al.*, in *Proceedings of the 14th International Conference on Cosmic Rays,* Munich, 1975, edited by K. Pinkau (Max-Planck-Institut, Garching, 1975), Vol. 8, p. 2861; B. S. Acharya *et al.*, in *Proceedings of the 17th International Cosmic Ray Conference,* Paris, 1981 (Centre d'etudes Nucleaires, Saclay, Gif-sur-Yvette, 1981), Vol. 11, p. 385; G. B. Yodh *et al.*, Phys. Rev. D **29**, 892 (1984).

[17]G. Thornton and R. W. Clay, Phys. Rev. Lett. **43**, 1622 (1979); Phys. Rev. D **23**, 2090 (1981); A. A. Andam *et al.*, in *Proceedings of the 17th International Cosmic Ray Conference* (Ref. 16), Vol. 11, p. 281; K. J. Orford and K. E. Turver, Nature (London) **264**, 727 (1976); R. Walker and A. A. Watson, J. Phys. G **7**, 1297 (1981); G. B. Yodh, in *First Aspen Winter Physics Conference,* proceedings, Aspen, Colorado, 1985, edited by M. M. Block (Ann. N.Y. Acad. Sci. 461) (New York Academy of Sciences, New York, 1986), p. 239.

[18]A. W. Wolfendale, Rep. Prog. Phys. **47**, 655 (1984).

[19]A. R. Bell, Mon. Not. R. Astron. Soc. **182**, 147 (1978); **182**, 443 (1978).

[20]R. D. Blandford and J. P. Ostreicher, Astrophys. J. **227**, L49 (1978).

[21]W. I. Axford *et al.*, in *Proceedings of the 15th International Cosmic Ray Conference,* Plovdov, Bulgaria, edited by B. Betev (Bulgarian Acad. Sci., Plovdov, Sofia, 1977), Vol. 11, p. 32.

[22]J. Ormes and P. Freier, Astrophys. J. **222**, 471 (1978).

[23]P. O. Lagage and C. J. Cesarsky, Astron. Astrophys. **18**, 289 (1982).

[24]A. M. Hillas, in *Proceedings of 16th International Cosmic Ray Conference,* Kyoto, Japan, 1979 (Institute of Cosmic Ray Research, University of Tokyo, Tokyo, 1979), Vol. 8, p. 7.

[25]G. T. Zatsepin, in *Proceedings of 8th International Cosmic Ray Conference,* Jaipur, India, 1963, edited by R. R. Daniels *et al.* (Tata Institute of Fundamental Research, Bombay, India, 1963), Vol. 4, p. 100.

[26]C. E. Fichtel and J. Linsley, Astrophys. J. **300**, 474 (1986).

[27]J. A. Wrotniak, SHOWERSIM, University of Maryland Report No. PP-85-18 (unpublished).

[28]F. E. Taylor *et al.*, Phys. Rev. D **14**, 1217 (1976).

[29]T. K. Gaisser and T. Stanev, in *18th International Cosmic Ray Conference, Bangalore, India, 1983, Conference Papers,* edited by N. Durgaprasad *et al.* (Tata Institute of Fundamental Physics, Bombay, 1983), Vol. 5, p. 174.

[30]Z. Wlodarcyzk *et al.*, in *Proceedings of the 17th International Cosmic Ray Conference* (Ref. 16), Vol. 5, p. 315.

[31]For references, see B. Rossi, *High Energy Particles* (Prentice Hall, New York, 1952), p. 251ff.

[32]J. Nishimura, in *Handbuch der Physik,* edited by S. Flugge (Springer, Berlin, 1967), Vols. 46 and 2; K. Greisen, Annu. Rev. Nucl. Sci. **10**, 63 (1960).

[33]A. M. Hillas and J. Lapikens, in *Proceedings of the 15th International Cosmic Ray Conference* (Ref. 21), Vol. 8, p. 460.

[34]G. Arnison *et al.*, Phys. Lett. **118B**, 167 (1982).

[35]A. I. Mincer *et al.*, Nucl. Instrum. Methods **A235**, 46 (1985).

[36]A. I. Mincer *et al.*, Nucl. Instrum. Methods **A238**, 482 (1985).

[37]G. B. Khristiansen *et al.*, in *18th International Cosmic Ray Conference, Bangalore, India, 1983, Conference Papers* (Ref. 29), Vol. 9, p. 195.

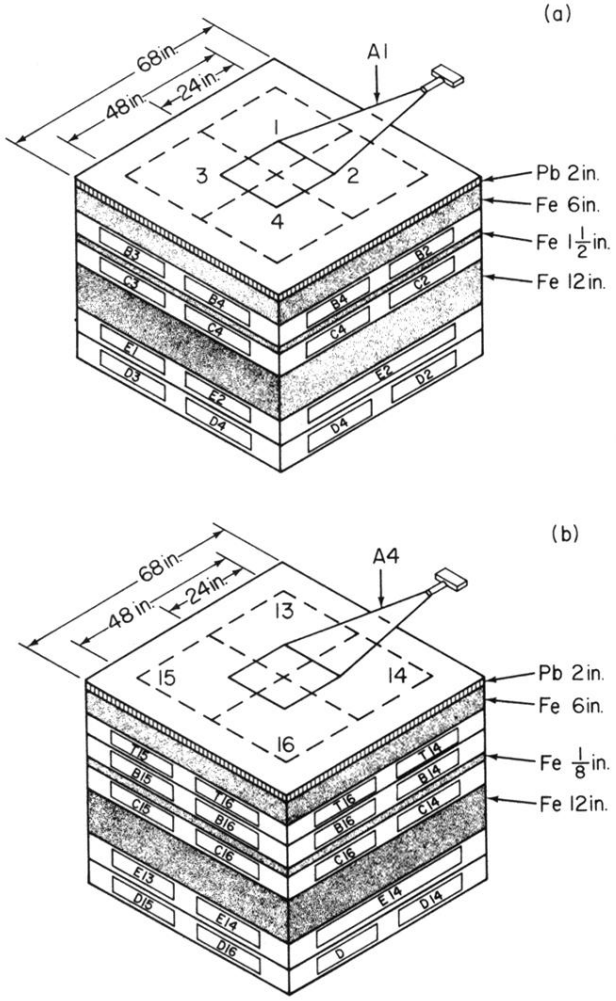

FIG. 2. Detail of the construction of the calorimeters I through III (a) and calorimeter IV (b).